DEUTSCHES ELEKTRONEN – SYNCHROTRON DESY

DESY SR 90-02
March 1990

X-Ray Standing Wave Analysis of Highly Perfect Cu Crystals and Electrodeposited Sub-Monolayers of Cd and Tl on Cu Surfaces

J. Zegenhagen, G. Materlik

Hamburger Synchrotronstrahlungslabor HASYLAB at DESY, Hamburg

W. Uelhoff

Institut für Festkörperforschung, KFA Jülich

ISSN 0723-7979

NOTKESTRASSE 85 · 2 HAMBURG 52

To be sure that your preprints are promptly included in the
HIGH ENERGY PHYSICS INDEX,
send them to the following address (if possible by air mail):

DESY
Bibliothek
Notkestrasse 85
2 Hamburg 52
Germany

DESY SR 90-02
March 1990

ISSN 0723-7979

X-Ray Standing Wave Analysis of Highly Perfect Cu Crystals and Electrodeposited Sub-Monolayers of Cd and Tl on Cu Surfaces

J. Zegenhagen* and G. Materlik
Hamburger Synchrotronstrahlungslabor HASYLAB at DESY,
Notkestr. 85, D-2000 Hamburg 52, W. Germany

W. Uelhoff
Institut für Festkörperforschung, KFA Jülich,
Postfach 1913, D-5170 Jülich, W. Germany

* now at: Max-Planck-Institut für Festkörperforschung, Heisenbergstr. 1,
D-7000 Stuttgart 80, W. Germany

submitted to Journal of X-Ray Science and Technology

ISSN 0723-7979

Abstract

Experimental requirements for measuring the structure and coverage of adsorbates in the monolayer regime on single crystals with X-ray standing wavefields are discussed in detail together with a thorough description of the theory. The near surface region of Cu crystals was probed depth selectively by detecting K as well as L fluorescence as a function of fluorescence escape angle. The effect of crystalline imperfections and of dispersive crystal arrangements on the spatial resolution of standing wave measurements is described. Copper crystals with (111) and (100) surface orientation were used as substrates for electrodeposition of Cd and Tl from an aqueous electrolyte using cyclic voltammetry. Submonolayer amounts of Cd and Tl deposited in the underpotential range were investigated on the emerged electrodes with X-ray standing waves keeping the samples under atmospheric pressure, in air or in inert atmosphere.

1. Introduction

More than 20 years have passed, since Battermann proposed to utilize an X-ray interference effect, occuring when reflecting a plane X-ray wave from a perfect crystal, for structural investigations of impurities in single crystals [1]. After about 10 years of scarce recognition by the physics community, an increasing number of publications over the last ten years has turned the so called X-ray standing wave (XSW) technique into an established tool in solid state physics. This was due to the boost in analyzation power by the use of synchrotron radiation sources [2] and the particular strength of the XSW technique in determining the structure of surface adsorbate systems with high spatial resolution in real space [3, 4,5]. Different from other scattering techniques like low energy electron diffraction (LEED) or surface X-ray diffraction (SXD), no phase information is lost in the XSW analysis [6]. Furthermore, the XSW technique is unambiguously element-specific.

As a limitation of the method was frequently seen that the XSW technique can only be applied to flawlessly perfect single crystals. Thus it was assumed that only few semiconductor crystals, such as Si and Ge, which exhibit a virtually perfect crystal structure could be used as specimens. However, this restrictions of the XSW technique is exaggerated which has been prooven in two different ways. Firstly it was demonstrated that other crystals than semiconductors (like Cu [7], GGG [8], $LiNbO_3$ [9]) can be grown perfectly enough to serve as substrates for XSW measurements. Secondly, modifications of the XSW technique were implemented which can (a) significantly relax the requirements on the substrate crystal structure or (b) even lift them completely. This is done in case of (a) by performing XSW measurements in backscattering geometry [10,11] while (b) is realized by using 0-th order Bragg reflection (total external reflection) or reflections from synthetic multilayer structures [12].

Either for intensity purposes or tunability of energy the use of synchrotron radiation is crucial for all these cases.

In the present study we use Cu-crystals as substrates. Some of the specimens were of unique quality (no dislocations) while others exhibited a moderate dislocation density. We show how we analyzed the crystal structure of these substrates and evaluate carefully, to which extent the observed defects may affect the interpretation of XSW data.

While we appreciate that it is increasingly recognized that the requirements on the crystal structure do not pose a serious limitation in the application of the XSW technique, oversimplification of the technical requirements should be avoided. One factor which can limit or destroy the resolution of the technique is often neglected and this is phase contrast and, intimately connected, dispersion. If an X-ray wave characterized by a certain volume in phase space, i.e. a spread in energy, angle and space, is reflected by a single crystal, the reflected energies are spread in space (dispersed). A rainbow-like X-ray wave is produced since Bragg's law requires a certain relationship between X-ray energy (wavelength) and angle of incidence, defined by the particular crystal and the selected diffraction planes. If such a dispersed X-ray wave is incident on a second crystal the whole wave is only reflected simultaneously from this crystal if there is a match between angle of incidence and energy for each individual spot on the crystal. This is ideally fulfilled only, if the two crystals are of the same kind, reflecting by the same diffraction planes and are in a parallel-, (+,-)-setting. We call this crystal arrangement non-dispersive. However, for XSW measurements non-dispersiveness is not sufficient to guarantee good contrast for the modulation of the X-ray interference field which serves as probe for the structure of atomic arrangements. Questions concerning dispersion and phase contrast will be discussed in more detail in section three of this paper.

In the main part of the paper we will report investigations with XSW on the structure of adsorbates on Cu surfaces: Tl on Cu(111) and Cd on Cu(111) and Cu(100). Since the measurements were performed under normal gas pressure (normal ambient or inert gas), some caution is advised in the interpretation of the results in comparison with measurements made under UHV conditions. However, monolayers of Tl on Cu(111) exhibit an unusual stability and no change in the XSW results was observed over periods of days while the specimens were kept under normal ambient conditions. The adsorbates were deposited by electrochemical methods and additional information on the deposits like binding energy, coverage and to some extend about the cleanliness of the substrate surface are obtained by cyclic voltammetric measurements.

Finally, in the appendix we will present a thorough description of the XSW analysis.

2. XSW Data Analysis

Only a brief description of the XSW analysis is given in this section and the interested reader is referred for more details to the appendix.

A standing wave pattern is excited by Bragg-reflecting a plane x-ray wave from a single crystal [13]. For an XSW measurement, the reflected beam intensity and the inelastic and diffuse scattering from the sample (e.g. fluorescence) is monitored simultaneously but independently as function of ϑ or λ while passing through the narrow range of strong Bragg reflection by tuning either the reflection angle ϑ of the sample (as in the present case) or the wavelength λ of the incident radiation. As shown

in the appendix, the yield Y_F of a particular fluorescence line can be expressed as

$$Y_F = I_F/I_F^o = e(\vartheta,\lambda)\{1+R(\vartheta,\lambda)+2\sqrt{R(\vartheta,\lambda)}f_{c,m}\cos[v(\vartheta,\lambda)-2\pi\Phi_{c,m}]\} \qquad (1)$$

with fluorescence intensity I_F, off-Bragg-intensity I_F^o, extinction prefactor $e(\vartheta,\lambda)$, reflectivity $R(\vartheta,\lambda)$, coherent fraction $f_{c,m}$, wavefield phase $v(\vartheta,\lambda)$, coherent position $\Phi_{c,m}$ and reflection order m. When the fluorescence arises from a thin surface layer, $e(\vartheta,\lambda) = 1$. If the fluorescence originates from substrate atoms or foreign atoms distributed isotropically within the substrate, $e(\vartheta,\lambda) = d_\vartheta/d_e \leq 1$, with d_ϑ as function of ϑ,λ (see equ. (A22)). Here d_ϑ is the extinction depth of the X-ray wavefield as a function of Bragg angle whereas d_e is the extinction depth for zero reflectivity.

A theoretical expression for $R(\vartheta,\lambda)$ equ. (A.10) is fitted with three free parameters (angular gain, angular offset, maximum reflected intensity) to the experimentally obtained reflectivity data. Since this determines the angular scale and because $R(\vartheta,\lambda)$ and $v(\vartheta,\lambda)$ are calculated from dynamical theory of X-ray diffraction (DTXD) [13], only four undetermined parameters are left in fitting ($Y_F I_F^o$) to the fluorescence intensity I_F recorded as a function of angle. If $e(\vartheta,\lambda) = 1$, only three parameters are left and I_F^o, $f_{c,m}$ and $\Phi_{c,m}$ are determined by such fit. In some cases mentioned below, e.g. when the Cu K substrate fluorescence was evaluated, $\Phi_{c,m}$ was fixed and $e(\vartheta,\lambda)$ varied via α (equ. A22) to determine the depth d_e sampled by the X-rays.

It is useful to relate $\Phi_{c,m}$ to a parameter z_A which is associated with the distances of the fluorescence selected atomic species normal to the diffraction planes via

$$z_A = (\Phi_c + n)\, d_h/m \qquad (2)$$

where d_h is the substrate diffraction plane spacing (for the first allowed reflection of a set of parallel diffraction planes) and n is an integer counting the multiples of the spacing. In general, z_A represents a weighted average of the distances of the entire number of sampled adsorbate atoms measured normal to the diffraction plane (compare equ. (A23) f.f.).

If the adsorbate atoms occupy a single site normal to the substrate diffraction planes, z_A gives this position directly.

3. XSW Measurement and Phase Contrast

Equ. (1) holds exactly only for a perfect plane wave incident on a perfect single crystal with a perfectly flat surface. In reality, the incident wave is a section of a spherical wave ("pseudo plane") and crystal and crystal surface exhibit defects. Before we present experimental investigations on the Cu-crystal lattice perfection, we will discuss in this chapter the effects of the X-ray optical properties of monochromators and samples on an XSW measurement.

A Du Mond diagram for an XSW crystal arrangement is shown as example in Fig. 1. The black trapezoid represents the emittance of the monochromator which illuminates the sample crystal (represented by the wide stripe with $\Delta\lambda_s$, $\Delta\vartheta_s$). The angular range $\Delta\vartheta_m$, transmitted by the monochromator, is at a synchrotron radiation source basically defined by the (small) angular divergence of the synchrotron x-ray beam (including effects of source and slit size). The width $\Delta\lambda_m$ of the stripe, and also in part $\Delta\vartheta_m$, is determined by the used monochromator crystals via the

widths of their single crystal reflection curves. The angular range $\Delta\vartheta_m$ and the width $\Delta\lambda_m$ can, for example, be reduced if one of the monochromator crystals is reflecting asymmetrically with grazing incidence. A particular value of $v(\vartheta,\lambda)$ defines a particular position of the wavefield nodal and antinodal planes with respect to the diffraction planes. As clearly visible, lines of equal phase $v(\vartheta,\lambda)$, giving the same position of the XSW pattern in the sample crystal, are consecutively excited by rotating either the monochromator double crystal arrangement relative to the sample, which will cause vertical movement in wavelength (λ-scan), or the sample crystal relative to the monochromator which will cause horizontal angular displacement of the sample curve (ϑ-scan). A third type of scan, also in the vertical direction, can be realized by changing the lattice parameter d of monochromator or sample via temperature or pressue (d-scan). Good resolution in $v(\vartheta,\lambda)$, i.e. small Δv, is obtained if $\Delta\vartheta_m \ll \Delta\vartheta_s$ and $\Delta\lambda_m \ll \Delta\lambda_s$.

Fig. 2 shows schematically three different crystal arrangements (Fig. 2a) and the corresponding Du Mond representations (Fig. 2b). At least two consecutive crystal reflections are commonly used in X-ray monochromators at a synchrotron radiation source. The direction in which $v(\lambda,\vartheta)$ changes by π rad across the stripes representing the acceptance of the samples is indicated by arrows. It is obvious that case I is best suited for an XSW measurement since it allows to perform λ- and ϑ-scans. Case II can only be used for λ scanning. In case III phase contrast can only be obtained at the wings of the rocking-curve. These different approaches and intermediate cases for XSW measurements can be selected via the photon wavelength, reflection vector, asymmetry factor [14, 6] and crystal material.

Finally, the influence of lattice imperfections on XSW measurements will be discussed. The requirements for the perfection of the crystal

lattice of monochromator or sample can be estimated from the derivative of Bragg's law

$$\Delta\lambda/\lambda = (\Delta\vartheta + \Delta\vartheta_i) \cot\vartheta + \Delta d/d \qquad (3)$$

In order to obtain the requested Δv, strain expressed by $|\Delta d| > 0$ and angular misalignment of different crystal areas ($\Delta\vartheta > 0$) or subgrains, ($\Delta\vartheta_i > 0$) have to be small. Strain and small angular spread (e.g. mosaic spread) in the sample are illustrated in a Du Mond diagram in Fig. 3. The emittance from the (perfect) monochromator is again represented by the black trapezoid. The curves in the insert represent schematically (λ,ϑ)-curves of the undistorted sample (1), a part of the sample strained by Δd (2) and a part of the sample tilted by $\Delta\vartheta_i$ (3). Thus, the Du Mond representation of the sample is given by three different stripes (1,2,3) since the undistorted, strained and tilted parts of the crystal are excited with a different phase (v_1, v_2, v_3) via the monochromator and the overall phase information is blurred by Δv. It is obvious that restricting the beam to a small area of the sample reduces the influence of imperfections and thus $\Delta\vartheta_i$ and possibly cures this problem. Strain effects, however, cannot always be eliminated by reduction to small sample areas.

4. Characterization of Crystalline Lattice Perfections

In our present study we have employed three different methods to characterize the Czochralski grown Copper single crystals. Namely, double crystal topography [15], double crystal rocking curve measurements, and XSW measurements analyzing the K and L fluorescence from the Copper substrates. All cylindrical Copper samples with diameters between 9 and 12 mm were single crystals, grown either in [111] or [100] direction. In order to avoid mechanical damaging from cutting and polishing they were

carefully electrolytically cut as well as electrolytically polished [16,17].

4.1 Double Crystal Topography

The experimental set-up used for topographic investigations is shown in Fig. 4. Two analog feedback stabilization units (MOSTAB) [18] were used to keep monochromator and sample crystals aligned in angle during exposure of a film. With a silicon (440) monochromator, copper (222) and (400) reflections were used for the (111) and (100) samples, respectively. A change of contrast of about 5% on the topographs recorded on the slope of the rocking curves at 50% reflectivity corresponds to strain or angular misalignment of $\Delta\vartheta/\vartheta = \Delta d/d \simeq 10^{-6}$. Fig. 5 shows topographs of small areas of two different Cu sample crystals which have a large difference in dislocation density (DD). Such topographs do not only show the effect of strain and dislocations but features of the topography of the surface of the crystal as well. If present, a curvature for instance will cause local changes of the asymmetry parameter within the area illuminated by the X-ray beam and will therefore not only affect the width and shape of the rocking curve but also locally the wavefield intensities.

4.2 Double Crystal Rocking Curves

Rocking curves of the crystal were measured by changing the angle of the sample crystal relative to the monochromator (ϑ-scan). Such curves are shown in Fig. 5c. As can be seen, a rounded, more symmetric top of the curve and an increase in intensity in the wings is an indication of the imperfection of the crystal. However, the width of the rocking curve itself is not a very sensitive measure of the perfection of the crystal.

4.3 XSW Substrate Fluorescence Measurement

A very sensitive method to characterize a crystal and its possible use as substrate for studying adsorbates with XSW measurements is the XSW analysis of the substrate fluorescence itself. The experimental set-up used for this purpose is shown in Fig. 6a. A NaI(Tl) detector and a Si(Li) solid state detector monitored the Bragg reflected X-ray beam and the scattered photons, respectively. Both signals were detected as a function of reflection angle ϑ within the angular range of the Bragg reflection. A comprehensive description of XSW fluorescence measurements is given in [19,2,6].

The measured angular dependence of the Cu K_α fluorescence yield is shown for two different crystals with different DD in Fig. 7. Measurements for two different take-off angles α (see Fig. 6b) are also illustrated. As seen from equ. (A22b), if sufficiently small, α mainly determines the depth over which atoms contribute to the fluorescence yield. Thus, if $\alpha = 10^o$ the mean sampled crystal depth $d_e = 1.7 \times 10^4$ Å, whereas for $\alpha = 0.8^o$, $d_e = 1800$ Å.

The data were given a least squares fit to equ. (1) using three fitting parameters I_F^o, α and f_c and setting $\Phi_c = 0$. For DD = 300 cm^{-2}, $f_c = 0.960 \pm 0.005$ was determined by the fit whereas $f_c = 0.91 \pm 0.02$ for DD = 2000 cm^{-2}. Since the theoretical value is $f_c = D_{W111} = 0.97$ [20] (see also equ. A31, A32), the influence of the dislocation density on f_c is clearly visible.

A measurement of the Cu-L fluorescence yield is illustrated in Fig. 8. Since the energy of the Cu L lines (0.9 keV) is much lower than that of the Cu-K_α line (8 keV), the absorption coefficient μ_a becomes large thus reducing the sampled depth d_e from which fluorescence reaches the

detector. For the examples shown, the fluorescence was measured with a take-off angle $\alpha = 8^o$ which corresponds to $d_e = 150$ Å. The χ^2-fit to the data gives $f_c = 0.67 \pm 0.04$ with $\Phi_c = 0.00 \pm 0.02$. The reduction of f_c by 31% in comparison to the ideal value 0.97 is a clear indication of a decrease in the lattice perfection closer to the surface because it was proven by topography that the crystal was dislocation-free. Since $\Phi_c = 0.00$ as expected, only shallow surface region are randomly disordered normal to the surface. This is in agreement with the observation that the coherent fraction of the adsorbates never exceeded 70%.

All of the methods discussed above were used to characterize the copper samples before using them as substrate for XSW measurements to study the structure of adsorbates. The chosen examples also demonstrate that these methods are not only valuable for characterization, but also as test for selecting proper crystals for XSW measurements. Even if modifications of the XSW technique are used allowing measurements on samples with less perfect crystalline lattice structure as discussed in the introduction, characterization techniques like those described above are almost a necessity.

5. Adsorbate Preparation and Cyclic Voltammetry (CVM)

Adsorbates were deposited on the surfaces by underpotential deposition (UPD) from an electrolyte. The adsorption process was monitored by linear sweep voltammetry with a set-up as shown in Fig. 9. The (111) or (100) faces of the cylindrical Cu single crystal rods (Cu) were immersed into the 0.5 Mol Na_2SO_4 electrolyte which contained either 1 mMol $TlNO_3$ or 1 mMol $CdSO_4$. The electrochemical glass cell was equipped with two side compartments for the platinum counterelectrode (C) and for the saturated Calomel reference electrode (R). A closed stopcock to the side

compartment with R prevented any significant exchange of chemical species while enabling low current transfer. Nitrogen (N_2) was flowing through the solution and the inner part of the cell to reduce the oxygen partial pressure in the solution. In order to prevent exposure of the emerging crystal to air, the electrolytical cell was additionally kept inside a glove bag with N_2 atmosphere during deposition of Cd. The voltage drop across the Cu electrolyte interface was controlled by a three-electrode potentiostat. Current-potential diagrams (voltammograms) were obtained with an x-y recorder.

The sample surface was cleaned initially by cycling the electrode potential periodically several times within the range limited by the onset of Cu oxydation on one side and bulk metal deposition on the other. The anodic and cathodic charges became balanced after several minutes cycling in an oxygen-free cell and solution. For XSW measurements, the sweep was stopped in the cathodic direction at a fixed potential and the sample was removed from the solution. During removal, care was taken to peel off the electrolyte completely.

Three anodic stripping curves, recorded immediately before removal of the sample, are shown in Fig. 10. Fig. 10b was recorded with trace amounts of oxygen in the cell atomosphere. Although not typical for this kind of preparation [7], the Tl stripping peak D is visible here.

Basically, the adsorbate coverage can be calculated from the voltammograms when the exposed Cu surface area and the sweep frequency are known. However, values for the double layer charging, the degree of charge transfer and the degree of surface roughness are in addition needed, but usually not accurrately known and thus coverages Θ_{UPD}, calculated from the voltammograms, exhibit relatively large margins of error.

From the potential difference $\Delta U = U_{SB}-U_{SU}$ between the potentials of bulk (U_{SB}) and UPD (U_{SU}) stripping peaks, the adsorbate binding energy E_{BA} can be calculated using $E_{BA} = e_o\Delta U + E_S$ with the electron charge e_o and the adsorbate bulk material binding energy (sublimation energy) E_S [22,23]. Additional information about the kinetics and the ordering of the adsorbate phase can be deduced from the peak half-width δU [23]. A large (narrow) peak width is expected for repulsive (attractive) adsorbate-adsorbate interaction. For Cd on Cu(111) ΔU = -0.29 V and δU = 90 mV, whereas ΔU = -0.20 V and δU = 90 mV for Cd on Cu(100). In the case of Tl on Cu(111) ΔU = -0.33 V and δU = 50 mV. Using sublimation energies [21] E_S = 1.88 eV and 1.16 eV for Tl and Cd, respectively, the adsorbate binding energies E_{BA} are 2.21 eV (Tl/ Cu(111)), 1.45 eV (Cd/Cu(111)) and 1.36 eV (Cd/Cu(100)).

6. X-Ray Standing Wave Measurements

The experimental set-up is shown in Fig. 6 and discussed in chapter 4.3. Cu crystals with dislocation densities < 2000 cm^{-2} were used as substrates with (100) and (111) surface orientation. The Si(Li) detector received photons from a 30 mm^2 illuminated surface spot in a solid angle of 0.1 sr. A Ge(220)/Si(220) slightly dispersive [2] double crystal monochromator was used. The XSW analysis of the Cu K fluorescence yield gave coherent fractions between 0.81 and 0.93 whereas ideally $f_c \simeq 0.97$. The reduction of f_c originates from the slight curvature of the crystal surface.

6.1 Cd on Cu(111)

Because of the reactivity of the Cd/Cu system with air, all samples were kept under protective atmosphere throughout preparation and XSW

measurement. A typical spectrum of scattered photons at a fixed reflection angle ϑ is shown in Fig. 11. Fig. 12 shows the Cu(111) reflectivity and the corresponding background corrected Cu L and Cd L fluorescence yields recorded as function of ϑ. The energy of the incident X-rays (E_γ) was 6.9 keV. From the spectra shown in Fig. 11, it is obvious that only negligible amounts of sulphur from the electrolyte remained on the emerged electrode crystals. The Cd coverage was determined by comparing the Cd L fluorescence intensity with the fluorescence intensity of an implanted standard sample.

Results of several measurements are compiled in Table 1. The phase Φ_c is converted into the distance $z_A = (1 + \Phi_c)d_H^{Cu}$, with $d_{111}^{Cu} = 2.09$ Å. All listed adsorbates were deposited at an electrode potential U_{SCE} = -0.7 V. However, comparable coverages Θ_{Cd} ($= \Theta_{Fl}$) also remained on the surface when the electrode was extracted at potentials positive with respect to the UPD peak position. No changes of f_c, Φ_c and Θ_{Cd} were observed when the sample was kept under He atmosphere during the XSW study. Exposure to air, however, produced variations of Φ_c and f_c with time. Also given in Table 1 are the values for f_c^{Cu} and Φ_c^{Cu} as determined from the analysis of the Cu substrate fluorescence. The reduced coherent fraction indicates some imperfections of the crystal in the surface region. However, the values Φ_c^{Cu} indicate that there is no systematic error involved in the analysis of adsorbate positions.

6.2 Cd on Cu(100)

Using for (100) surfaces the same procedure (inert He atmosphere) as described for the measurement of Cd layers on (111) surfaces produced coherent fractions up to 30% ($f_c = 0.3$) but gave no consistent results in Φ_c. If exposed to open air, coherent fractions as high as 0.3 dropped to zero immediately, demonstrating the high reactivity of this interface.

6.3 Tl on Cu(111)

Tl layers were prepared in oxygen-free electrolytes as well as electrolytes containing trace amounts of oxygen. After extraction of the electrode, the layers exhibited no structural changes in air and all XSW measurements were performed under normal ambient conditions. The primary photon energy was $E_\gamma = 15.3$ keV and a 0.4 mm thick Al adsorber was placed in front of the Si(Li) detector to prevent the data acquisition system from being overloaded by the strongly excited Cu K fluorescence radiation. The coverage Θ_{Tl} ($= \Theta_{Fl}$) was determined with the help of equ. [A38] by using the off-Bragg substrate fluorescence intensity as a reference.

Results of several measurements are compiled in Table 2 and shown in Fig. 13. For the case of an oxygen-free electrolyte, Tl was deposited at a potential of -0.57 V. With an oxygen containing electrolyte, the potential for deposition before extraction ranged from -0.33 V to -0.83 V. As for the case of Cd on Cu, adsorbates of Tl were also detected on the Cu surface when the electrode was extracted at potentials positive with respect to U_{SCE} = -0.50 V, which marked the position of the UPD peak and appeared to be the same when oxygen was present in the solution. When the Tl adsorbate was rinsed with water right after electrode extraction, the total Tl coverage Θ decreased whereas the coherent coverage $\Theta_c = \Theta \cdot f_c$

and the phase Φ_c remained constant. This clearly shows that only randomly distributed Tl was removed by the water rinse.

7. Discussion

The XSW measurements reveal that sizeable amounts of the adsorbate were already deposited on the surface when the electrodes were held at a potential positive with respect to the UPD peaks. This can best be seen by preparations 3,4,5 of the Tl adsorption. However, the adsorbate position z_A as determined by XSW did not differ significantly from the result z_A from other preparations. Note in this context, that the coverage Θ_{UPD} determined by CVM was always smaller than Θ_{Fl} determined by fluorescence analysis of the emerged electrodes.

This indicates a strong gradient in the concentration of metal ions in the inner Helmholtz layer in a potential range positive with respect to the UPD peak. As a result of the equilibrium condition at the solid-electrolyte interface, the metal ions may already be physisorbed or even stronger specifically adsorbed on the electrode surface at potentials where no charge transfer is observed by CVM. Strong evidence for specific ionic adsorption at potentials positive with respect to the UPD peak has also been found for Tl on Ag by Second Harmonic measurements [24]. However, for the present case only an in-situ measurement can separate out the effect of the electrode extraction.

The difference in stability of the three systems in oxygen atmosphere can directly be related to the experimentally determined binding energies. Cd on Cu(100) with the lowest E_B = 1.36 eV is most unstable and exposure to air led to rapid random disorder. Cd on Cu(111) with E_B = 1.45 eV was stable in inert gas but showed a response to air

which finally led to disorder. Tl on Cu(111) with largest E_B = 2.21 eV was stable in air and even water did not affect the measured adsorbate position.

An explanation is needed for the fact that the total coverages of all adsorbates remained well below 1 ML and that total and coherent coverage varied for different preparations with the same applied potential before electrode extraction. The surface of the Cu sample was electrolytically polished in standard grade H_3PO_4 and impurities may have been left on the surface which possibly were not removed by cycling the potential as described above. CVM performed with Cu(111) grown on mica under ultra clean conditions in UHV yielded higher coverages and more pronounced, sharper peaks in the voltammograms [25]. The disorder of the substrate revealed by XSW analysis of the substrate fluorescence can also indicate roughening of the Cu surface due to the process of electrolytically cycling [26] and may have given rise to some adsorption on random surface sites.

In order to discusss structural models for the UPD overlayers, the binding geometry for high symmetry sites on Cu(111) are plotted in Fig. 14. Bond lengths (Table 3) were calculated for comparison from averaged z_A values by assuming an unrelaxed Cu surface and metallic radii for Cu, Cd and Tl. Appendix A2 summerizes the used constants and equations.

For the Tl/Cu(111) interface, Table 3 (column 2) shows that a one-fold adsorption site can be excluded since it would require a 11% compression of the Cu-Tl bond length (= sum of metallic radii). A distinction between an exclusively twofold (A2) and an exclusively threefold (A3) site, however, cannot be made from the results of the measurements. Thus, an occupation of both sites with equal weight as

shown in Fig. 15 is also possible. This one dimensional chain model is similar to the arrangement found on Cu(100) [27,28].

Trace amounts of oxygen in the electrolyte change the Cu(111) surface structure. The smaller z value of the Tl atom relative to the Cu surface can be explained by an -0.4 Å inward relaxation of the top Cu layer relative to the bulk diffraction planes [29,7]. However, a different model involving oxygen incorporation below the top Cu layer in a threefold site [30] is also consistent with the XSW measurement.

For Cd/Cu(111) the onefold site can also be excluded. Between sites A2 and A3 and mixtures of both, however, cannot clearly be distinguished from the measurements. A similar discussion holds as for the Tl/Cu(111) overlayer. Note, however, that the larger stripping peak half width δU_{Cd} = 90 mV in comparison to δU_{Tl} = 50 mV indicates a less attractive Cd-Cd interaction in the overlayer, making a chain like structure as in Fig. 15 of the Cd less and a single site occupation more likely.

8. Conclusion

Czochralski grown Cu single crystals were studied with double crystal diffractometry, high resolution topography and X-ray standing wave analysis. Although dislocation-free crystals can be prepared, it was demonstrated in addition that high resolution XSW analysis can be carried out using substrate crystals which have a moderate dislocation density.

Overlayers of Tl and Cd on Cu(111) and Cd on Cu(100) were prepared by underpotential deposition. Since high coherent fractions were measured with XSW fields, it can be concluded that the distribution functions describing the position of the adsorbates normal to the surface have

sharp maxima indicating preferential adsorption sites. This means, that Tl and Cd at coverages < 1 ML form ordered phases on Cu(111) which are stable at atmospheric gas pressure.

Binding energies were deduced from voltammetric measurements and were used to explain the different stability of the layers when exposed to air. For the Tl/Cu(111) system the dependence of the adsorbate structure on the surface oxydation state of Cu in the electrolyte was clearly demonstrated. For the geometrical structure of the Cd and Tl/Cu(111) interfaces, adsorption on a onefold on top site is excluded. The results are consistent with models using twofold and/or threefold adsorbate sites. However, measurements of other Fourier components, specially those in directions tilted relative to the surface, are needed to determine the lateral structure in more detail.

Acknowledgement

We would like to thank Professor D.M. Kolb and Dr. G. Piazza for valuable advice on electrochemistry as well as for the loan of the equipment to carry out the cyclic voltammetry, and A. Fattah for his skillful help in preparing the Cu crystals. The project was supported by the German Federal Minister for Science and Technology.

Table 2. XSW results of Tl on Cu(111) measurements.

	prep. no.	potential vs SCE (V)	H_2O rinse	Θ_{Fl} (ML)	f_c	position z_A norm.(111) (Å)	$\Theta_c = f_c \Theta_{Fl}$ (ML)	Θ_{UPD} (ML)	Θ_{Fl}/Θ_{UPD}
a)	1	-0.55		0.32	0.21±0.03	2.39±0.04	0.07		
	2	-0.55		0.37	0.28±0.03	2.42±0.03	0.10		
	3	-0.33	x	0.13	0.49±0.04	2.37±0.03	0.06		
	4	-0.41	x	0.05	0.66±0.06	2.25±0.03	0.03		
	5	-0.48		0.14	0.33±0.04	2.22±0.06	0.05		
	6	-0.59		0.22	0.25±0.03	2.27±0.06	0.06		
	7	-0.60		0.24	0.26±0.04	2.26±0.06	0.06	0.26	1
	7	-0.60	x	0.08	0.65±0.11	2.31±0.05	0.05		
	8	-0.70		0.27	0.19±0.03	2.29±0.07	0.05		
	9	-0.77		0.35	0.24±0.04	2.34±0.06	0.08		
	10	-0.83		0.38	0.17±0.04	2.41±0.08	0.06		
b)	1	-0.57		0.31	0.11±0.04	2.72±0.06	0.03	0.17	1.8
	2	-0.57		0.16	0.40±0.06	2.68±0.02	0.06	0.16	1
	3	-0.57		0.13	0.63±0.08	2.65±0.02	0.08	0.14	1

a) preparations performed out of O_2 containing electrolyte

b) " " " " O_2 free electrolyte

Table 1

Cd on Cu(111) results of measurements.

prep. no.	Θ_{UPD} (ML)	Θ_{Fl} (ML)	f_c	Φ_c	z_A (Å)	f_c^{Cu}	Φ_c^{Cu}	Θ_{Fl}/Θ_{UPD}
1			0.28 ±0.08	0.14 ±0.04	2.38 ±0.08			
2	0.2	0.2	0.48 ±0.03	0.13 ±0.01	2.36 ±0.02	0.74 ±0.05	0.01 ±0.02	1
3	0.06	0.1	0.24 ±0.03	0.14 ±0.02	2.38 ±0.04	0.66 ±0.04	0.00 ±0.02	1.7

Table 3: Results on Cu(111); Cu-Tl and Cu-Cd bond lengths l_A calculated from the XSW results for three different adsorption sites.

	1.		2.		3.	
Position	l_A [Å]	$\Delta l_A/l_A^M$	l_A [Å]	$\Delta l_A/l_A^M$	l_A [Å]	$\Delta l_A/l_A^M$
Onefold, A1	2.27	-25%	2.67	-11 %	2.37	-14 %
	(2.67)	(-11%)				
Twofold, A2	2.61	-13%	2.96	-2 %	2.69	-3 %
	(2.96)	(-2%)				
Threefold, A3	2.71	-10%	3.05	+1.3%	2.79	+0.7%
	(3.05)	(+1%)				

The bond lengths, l_A, resulting from the different adsorption sites, are calculated using eqs. A39-41 and taking for z_{Ai} the experimentally determined, averaged values z_A. Additionally listed are the thus resulting relative changes $\Delta l_A/l_A^M$ in bond length with l_A^M = 3.01 Å and 2.77 Å for Tl and Cd, respectively. The used symbols l_A, l_A^M and Δl_A are defined in appendix A2. Column 1: UPD of Tl on Cu(111) out of oxygen-containing electrolyte with z_A = (2.27±0.04)Å (Θ_{Tl} < 0.3 ML, no rinse [7]). In brackets are noted the results calculated for an inward relaxation of the Cu(111) surface by 0.4 Å. Column 2: UPD of Tl on Cu(111) out of oxygen-free electrolyte with z_A = (2.67± 0.02)Å (Θ_{Tl} < 0.3 ML). Column 3: UPD of Cd on Cu(111), out of oxygen-free electrolyte with z_A = (2.37±0.02)Å.

Figure Captions

Fig. 1 Crystal arrangement at a synchrotron radiation source in the Du Mond representation. The phase difference $v(\vartheta,\lambda)$ between the reflected and incident X-ray waves E_H and E_O respectively is constant along the thin lines within the broad stripe which represents the sample crystal reflection band. The black trapezoid is the emittance from the monochromator. Good modulations of the wavefield intensity within the lattice unit cell requires a small Δv in which case Φ_c and f_c (Eq. 1) can be determined with high precision. The shown case basically represents a parallel or (+,-)-setting but the diffraction spacings of sample and monochromator, d_{hs} and d_{hm} respectively, are different. However, since $\Delta\vartheta_m$ is small enough, such slightly dispersive arrangements denoted as (+(-),-) can be used routinely at synchrotron radiation sources.

Fig. 2 a) Three different crystal arrangements at a synchrotron radiation source. The first monochromator crystal m1 is reflecting symmetrically and the second one (m2) asymmetrically [14]. For case I and III the d-spacing of monochromator (m2) and sample (S), d_m and d_s respectively, are matching well and thus $\vartheta_m \simeq \vartheta_s$. For case II, λ_m is chosen such that ϑ_s is large, preferably $\simeq 90^o$.

b) The same crystal arrangements in the Du Mond representation. The emittance from the monochromator is given by the black trapezoid. The direction in which $v(\vartheta,\lambda)$ changes by π rad is indicated.

Fig. 3 Du Mond representation of subgrain angular misalignment and lattice strain. 1 : ideal case (d_h, ϑ_B); 2 : strained lattice ($d_h+\Delta d$, ϑ_B); 3 : misaligned grain (d_h, $\vartheta_B+\Delta\vartheta_i$). The inset shows the whole Du Mond plot but case 2 and 3 are exaggerated.

Fig. 4 Experimental set-up for double crystal topography. Three slits (S1, S2, S3) confine the synchrotron X-radiation beam from the storage ring DORIS. An electronic analog feedback circuit [18] (MOSTAB) senses the output of ionization chamber (I1) and drives a piezo crystal to keep the monocchromator crystals aligned. A second MOSTAB senses the output of the NaI-detector and keeps the sample crystal at ≅ 50% reflectivity during exposure of the film. Distance from monochromator to sample 200 cm; distance from sample to film 6 cm. Normally the film plane is placed parallel to the sample surface.

Fig. 5 a,b) Topographs from two different Cu crystals. The sections shown correspond to 0.6x0.6 mm^2 surface area. (222) reflection, E_γ = 8.6 keV. c) shows the Cu(222) reflection curves taken for the same spots as shown in a and b. Dislocation densities are about 300 cm^{-2} and 20000 cm^{-2} for 2a and b, respectively. o,+ exp. data points for a,b respectively; --- theoretical rocking curve fitted in width and height to data points; FWHM = 37 μrad.

Fig. 6 Sample environment in an XSW measurement. The arrangement from DORIS up to the ionization chamber is as shown in Fig. 4 with proper crystals X1, X2 selected for XSW measurements. In special cases a filter (A) was used in front of the Si(Li).
b) Detector geometry; note, that the Si(Li) detector (Det 2) is usually placed as shown in part a), looking almost into the

direction of the polarisation vector of the incoming σ polarized SXR.

Fig. 7 XSW measurement of Cu K fluorescence radiation from an illuminated Cu surface area of 2.5 mm^2. Measured (+++) and calculated (•••) Cu(111) reflection curve; (ooo) experimentally determined fluorescence yield; (——) fit to the experimental points.
Two different dislocation densities DD and take-off angles α were used.

Fig. 8 XSW measurement of Cu L fluorescence yield; symbols as in Fig. 7. A surface spot of ≅ 30 mm^2 was illuminated during the XSW scan.

Fig. 9 Electrolytical cell and experimental set-up for cyclic voltammetric measurements. Pot. = potentiostat, Rec. = X-Y recorder, R = reference electrode, C = counter electrode.

Fig. 10 Anodic stripping curves. The bulk stripping peak is marked by M and the UP stripping peak by D. A prebulk stripping peak (P in Fig. 10b) was observed for Tl if M was not too large. The high increase of current in 10b) for U > -0.4 V was typical if oxygen was present (compare Ref. 7).

Fig. 11 Part of a spectrum of 512 channels total, recorded by the Si(Li) and stored in the MCA for a particular angle ϑ ($\vartheta-\vartheta_B$ ≅ 120 μrad in Fig. 12). A section is multiplied by a factor 5.

Fig. 12 Measured and calculated XSW reflectivity (+++,•••) and Cd L (ooo,——) and Cu L (xxx,---) fluorescence yield curves.

Fig. 13 XSW results for Tl on Cu(111)

: preparations out of oxygen-free electrolyte.

o : preparations out of oxygen-containing electrolyte.

o : preparations out of oxygen-containing electrolyte and rinsed after electrode extraction with H_2O.

For $\Theta_{Tl} > 1$ ML the Tl position shifts to higher values.

Fig. 14 Binding geometries on Cu(111) in a) side and b) top view. One-fold (A1), twofold (A2), threefold (A3) positions and the corresponding distances z_{Ai} (i = 1, ..,3) to the surface. r^M_{Cu} is the metallic Cu radius.

Fig. 15 Model for Tl adsorbate structure on Cu(111). If the Tl is located precisely at A2 and A3, the Tl-Tl bond length is reduced by 4% compared to the metallic Tl-Tl bond length. If all chains are aligned parallel, the saturation coverage is 0.4 ML.

References

1 B.W. Batterman, Phys. Rev. Lett. 22, 703 (1969)

2 G. Materlik, J. Zegenhagen, Physics Lett. 104A, 47 (1984)

3 P. Funke, G. Materlik, Solid State Comm. 54, 921 (1985)

4 S.M. Durbin, L.E. Berman, B.W. Batterman, J.M. Blakeley, Phys. Rev. B 33, 4402 (1986)

5 J.R. Patel, P.E. Freeland, J.A. Golovchenko, A.R. Kortan, D.J. Chadi, Guo-Xin Quian, Phys. Rev. Lett. 57, 3077 (1986)

6 N. Hertel, G. Materlik, J. Zegenhagen, Z. Phys. B 58, 199 (1985)

7 G. Materlik, J. Zegenhagen, W. Uelhoff, Phys. Rev. B, Rapid Comm. 32, 5502 (1985)

8 S. Lagomarsino, F. Scarini, A. Tucciarone, Phys. Rev. B 29, 4859 (1984)

9 B.N. Dev, G. Materlik, to be published

10 T.Ohta, Y. Kitajima, H. Kuroda, T. Takahashi, S. Kikuta, Nucl. Instr. Meth. A 246, 760 (1986)

11 D.P. Woodruff, D.L. Seymour, C.F. Mc. Conville, C.E. Riley, D.M. Crapper, N.P. Prince, R.G. Jones, Phys. Rev. Lett. 58, 1460 (1987)

12 M.J. Bedzyk, D.H. Bilderback, G.M. Bommarito, M. Caffrey, J.S. Schildkraut, Science 241, 1788 (1988)

13 M. v. Laue, RÖntgenstrahlinterferenzen, Akad. Verlagsanstalt, Frankfurt/Main (1960)

14 M. Renninger, Z. Naturforsch. 16a, 1110 (1961)

15 U. Bonse, E. Kappler, Z. Naturforsch. 13a, 792 (1958)

16 H. Fehmer, W. Uelhoff, Journal of Scientific Instr. 2, 771 (1969)

17 H. Fehmer, W. Uelhoff, Journal of Scientific Instr. 2, 767 (1969)

18 A. Krolzig, G. Materlik, M. Swars, J. Zegenhagen, Nucl. Instr. Meth. 219, 430 (1984)

19 A. Krolzig, G. Materlik, J. Zegenhagen, Nucl. Instr. Meth. 208, 613 (1983)

20 D_{Will} is calculated with the help of Equs. (A31) and (A32). The mean square vibrational amplitude $\langle u^2 \rangle$ is calculated [13] from the Debye temperature Θ_D = 343 K [21].

21 C. Kittel, Einführung in die Festkörperphysik, R. Oldenburg Verlag München, Wien 1980

22 H. Gerischer, D.M. Kolb, J.K. Sass, Advances in Physics 27, 27 (1978)

23 D.M. Kolb in: Advances in Electrochemistry and Electrochemical Engineering 11, 125 (1978), ed. H. Gerischer, Wiley & Sons

24 G.L. Richmond, J.M. Robinson, V.L. Shannon, Progress in Surf. Sci. 28, 1 (1988) and references therein

25 G. Piazza, J. Zegenhagen, unpublished results

26 See, e.g., [24] and references therein

27 C. Binns, C. Norris, Surface Science 115, 395 (1982)

28 C. Binns, C. Norris, S.J. Gurman, J. Phys. C 16, 417 (1983)

29 H. Niehus, Surface Science 130, 41 (1983)

30 G. Materlik, M. Schmäh, J. Zegenhagen, W. Uelhoff, Phys. Chem. 91, 292 (1987)

APPENDIX

A1 XSW Data Analysis

A1.1 Calculation of reflectivity, phase and wavefield intensity

Following the well established concepts of dynamical theory of x-ray diffraction (DTXD) [13], interference between the incoming and reflected x-ray waves gives rise to a planar wavefield parallel to and periodic with the diffraction planes if a plane x-ray wave is Bragg reflected by a perfect single crystal. In the condition of Bragg reflection the photon wavefield resonantly adopts the spacing of the $\underline{H}$ Fourier component of the charge density distribution function if $\underline{H}$ is the diffraction vector giving rise to the reflection under consideration. The charge density ρ as a lattice periodic function can be represented as a Fourier series (vector symbols are omitted in subscripts)

$$\rho(r) = \sum_H \rho_H \exp(-2\pi i \underline{H} \cdot \underline{r}) \qquad (A1)$$

The effect of anomalous dispersion on the scattering process leads from the charge density to the complex scattering density $\rho_s(\underline{r})$

$$\rho_s(\underline{r}) = (1/V_c) \sum_H F_H \exp(-2\pi \underline{H} \cdot \underline{r}) \qquad (A2)$$

which is thus related to the structure factor F_H and determines in part the wavefield position. The volume of the lattice unit cell is V_c.

The diffraction vector $\underline{H}$ is related to the reciprocal lattice vector $\underline{G}$ by $\underline{H} = \underline{G}/2\pi$. The photon wavefield inside the crystal can be described as a Bloch wave. The weak interaction of x-rays with matter has the

convenient consequence that this Bloch wave consists, in the (2-beam) case of Bragg reflecting a linearly polarized plane wave, of two partial waves $\underline{E}_O(\underline{D}_O)$ and $\underline{E}_H(\underline{D}_H)$. Polarized means here either polarized in the plane of incidence (π-polarized) or normal to the plane of incidence (σ-polarized). The amplitude of the electric field of the incident and outgoing waves outside the crystal are described by $\underline{E}_O$ and $\underline{E}_H$, respectively, whereas $\underline{D}_O$ and $\underline{D}_H$ describe the electric displacements inside the crystal. Because we will restrict ourselves in the text on reflecting σ-polarized x-rays, we will treat $\underline{E}$ and $\underline{D}$ from now on as scalar quantities. The phase $v(\vartheta,\lambda)$ between the complex amplitudes $E_O(D_O)$ and $E_H(D_H)$ can be changed by π radians within the range of Bragg reflection by changing either the reflection angle ϑ or the wavelength λ of the incident radiation by $\Delta\vartheta$ and $\Delta\lambda$, respectively. From the well known Bragg equation

$$2d_h \sin\vartheta_B = m\lambda \tag{A3}$$

and if we assume for the crystal $\Delta d/d = 0$, with

$$\Delta\lambda = 2d_h m^{-1} \Delta\vartheta\cos\vartheta_B \tag{A4}$$

the equivalence of $\Delta\lambda$ and $\Delta\vartheta$ for performing XSW scans is obvious, as long as λ is chosen not too close to an absorption edge and ϑ_B not close to 90^o. Even within the dynamical theory of x-ray diffraction, Bragg's equation is valid to a good approximation although the true range of total reflection appears at a slightly larger angle than predicted by this simple equation. In (A3) and (A4) d_h is the spacing of the diffraction planes of the first allowed reflection for a set of parallel diffraction vectors $\underline{h}_m$ and m is the reflection order. In the above presented study $d_h = d_{111}$ or $d_h = d_{200}$ are the Cu(111) and Cu(200) lattice plane spacing and $m = 1$ and we generated an x-ray interference field

(standing wave) by Bragg reflecting from the (111), or (200) diffraction planes of the Cu substrate which are parallel to the surface of the crystals. The wavefield exists on both sides of the interface. Inside the crystal the wavefields extension is characterized by the extinction depth and the size of the x-ray beam. Outside the crystal the wavefield is limited to the region of overlap between E_O and E_H. A more stringent limitation, however, to which distance the wavefield extends into the region outside of the crystal is given by the coherence length of the used x-rays.

The above mentioned Bloch wave can be written as

$$E = \exp[2\pi i(\nu t - \underline{k}_O \cdot \underline{r})]\{E_O + E_H \exp[-2\pi i(\underline{H}\cdot\underline{r})]\} \tag{A5}$$

where ν is the frequency of the electromagnetic x-ray wave, $\underline{r}$ is a position vector and $\underline{k}_O$ is the vector of propagation of the incident x-ray wave. The ratio of the amplitudes of the x-ray waves is in our case given with the mentioned restrictions by

$$E_H/E_O = D_H/D_O = \eta \pm (\eta^2 - 1)^{1/2} \tag{A6}$$

where

$$\eta = [(\vartheta_B - \vartheta)\sin(2\vartheta_B) - \chi_O]/\chi_H \tag{A7}$$

The complex O and $\underline{H}$ Fourier components of the electric susceptibility χ are related to the structure factor via

$$\chi_{H,O} = \Gamma F_{H,O} \tag{A8}$$

with

$$\Gamma = (r_o\lambda^2)/(\pi V_c) \tag{A9}$$

where λ is the x-ray wavelength and r_o is the classical electron radius. We introduce the reflectivity $R(\vartheta,\lambda)$ with

$$R(\vartheta,\lambda) = |E_H|^2/|E_o|^2 \tag{A10}$$

and the normalized wavefield intensity i_W via

$$i_W = |E|^2/|E_o|^2 \tag{A11}$$

We choose z in direction parallel to $\underline{H}$ which means that in our case the z-direction is pointing outward the crystal, normal to the (111) or (200) surface. Furthermore, in case of the cubic Cu lattice we write

$$|\underline{H}| = m/d_h \tag{A12}$$

Now we can transform (A11) with (A5), (A10) and (A12) for the wavefield intensity to

$$i_W = 1 + R(\vartheta,\lambda) + 2\sqrt{R(\vartheta,\lambda)}\,\cos[v(\vartheta,\lambda)-2\pi mz/d_h] \tag{A13}$$

For the wavefield inside the crystal the intensity is

$$i_{WC} = i_W \exp[-z(\mu_\vartheta+\mu_e)(\sin\vartheta)^{-1}] \tag{A14}$$

Here μ_e is the linear coefficient of absorption for the used x-rays in Cu whereas

$$\mu_\vartheta = \mu_{AA} + \mu_{PE} \tag{A15}$$

accounts for the decay of the wavefield inside the crystal due to anomalous absorption (μ_{AA}) and primary extinction (μ_{PE}). Those coefficients are given by

$$\mu_{AA} = -(2\pi/\lambda)\chi''_H\,\mathrm{Re}(D_H/D_o) \tag{A16}$$

and

$$\mu_{PE} = -(2\pi/\lambda)\chi'_H\,\mathrm{Im}(D_H/D_o) \tag{A17}$$

with

$$\chi_H = \chi'_H + i\chi''_H \tag{A18}$$

With the above mentioned phase v which is variable by π radians, E_o and E_H are related via

$$E_H = \sqrt{R(\vartheta\lambda)}\;|E_o|\,\exp[iv(\vartheta,\lambda)] \tag{A19}$$

It is easy to see from (A13) that the wavefield intensity is modulated in z-direction and the period is given by d_h/m. Within the framework of dynamical theory of x-ray diffraction, $R(\vartheta,\lambda)$ and $v(\vartheta,\lambda)$ are for a chosen crystal, x-ray wavelength and $\underline{H}$ determined by the complex 0 and $\underline{H}$ component χ_o and χ_H, respectively, of the complex, lattice periodic electric susceptibility $\chi(\underline{r})$. The quantity χ_H in particular determines the limits for the π rad variation of $v(\vartheta,\lambda)$ and thus the position of the standing wavefield planes relative to the crystal lattice unit cell. For a known structure, like Cu, χ_o and χ_H can be calculated and thus $R(\vartheta,\lambda)$ and $v(\vartheta,\lambda)$ as a function of ϑ and λ where $v(\vartheta,\lambda)$ is given by

$$v(\vartheta,\lambda) = \arctan[\mathrm{Im}(D_H/D_o)/\mathrm{Re}(D_H/D_o)] \tag{A20}$$

A1.2 Analysis of XSW fluorescence data

Treating the photoelectric process for core levels in the dipole approximation means that the probability for the occurance of an x-ray absorption process is proportional to the wavefield intensity at the center of the scattering atom located at $z = z_A$. Here z measures a distance normal to the diffraction planes, i.e. parallel to $\underline{H} = m\underline{h}$ being the diffraction vector. The first allowed reflection of a parallel set of diffraction planes is characterized by $\underline{h}$ with the corresponding diffraction plane spacing d_h. Within the timeframe of an XSW measurement the radiative decay of such a core hole is instantaneous. If we consider now a large number of specific atoms (typically larger 10^{10}) residing at identical positions z_A whereas the lateral distribution can be arbitrary, the normalized fluorescence intensity, i.e. fluorescence yield Y_{FA} is given by

$$Y_{FA}^{h,m} = I_{FA}/I_{FA}^{o} \qquad \text{(A21 a)}$$

$$= 1 + R(\vartheta,\lambda) + 2\sqrt{R(\vartheta,\lambda)}\,\cos[v(\vartheta,\lambda)-2\pi m z_A/d_h] \qquad \text{(A21 b)}$$

for fluorescence from adsorbate atoms, and by

$$Y_{FS}^{h,m} = I_{FS}/I_{FS}^{o} = (d_\vartheta/d_e)Y_{FA}^{h,m} \qquad \text{(A21 c)}$$

for fluorescence from substrate atoms, where $I_{FA,S}^{o}$ denotes in either case the off-Bragg fluorescence intensity and $I_{FA,S}$ the fluorescene intensity as function of (ϑ,λ).

The angular dependent sampled thickness d_ϑ is given by

$$d_\vartheta = ((\mu_\vartheta+\mu_e)(\sin\vartheta)^{-1} + \mu_a(\sin\alpha)^{-1})^{-1} \qquad \text{(A22 a)}$$

and the sample thickness contributing fluorescence under off-Bragg (zero reflectivity) condition by

$$d_e = (\mu_e(\sin\vartheta)^{-1} + \mu_a(\sin\alpha)^{-1})^{-1} \qquad \text{(A22 b)}$$

Here μ_a is the absorption coefficient of the substrate material for the substrate fluorescence.

We realize from (A21) that an atom residing at position z_A+nd_A, where n is an arbitray integer, would give the same response as function of ϑ or λ. If we now allow arbitrary positions z_{Ai} (integer i, $1 \le i \le N_A$) and usually $N_A > 10^{10}$, then I_{FA} will represent a sum of N_A cos-functions with different phases determined by z_{Ai}, and we obtain

$$Y_{FA}^{h,m} = 1+R(\vartheta,\lambda)+2\sqrt{R(\vartheta,\lambda)}\,\frac{1}{N_A}\sum_{i=1}^{N_A}\cos(v(\vartheta,\lambda)-2\pi m z_{Ai}/d_h) \qquad \text{(A23 a)}$$

which will then result in an expression given by equ. (1) with amplitude $f_{c,m}$ and phase $\Phi_{c,m}$ with $f_c,\Phi_{c,m}$ from 0 to 1. Already because N_A is such a large number, we can exchange the summation with an integration where a normalized function P(Z) gives the real distribution of the contemplated atoms in z-direction. The angular dependent fluorescence yield as result of an XSW measurement [6] can thus be described as

$$Y_{FA}^{h,m} = 1+R(\vartheta,\lambda)+2\sqrt{R(\vartheta,\lambda)}\int P(z)\cos(v(\vartheta,\lambda)-2\pi m z/d_h)dz \qquad \text{(A23 b)}$$

Two corresponding equations are obtained for $Y_{FS}^{h,m}$ describing the fluorescence yield from substrate or generally isotropically distributed atoms within the bulk of the crystal. Both (identical) equations (A23,a,b) have a solution of the form given by equ. (1).

Usually the analysis of XSW data is performed by taking a reasonable model for the distribution function P(z), of atoms under consideration. Noting

$$P_m = \int \cos(2\pi m\, z/d_h)\, P(z)\, d_z \qquad \text{(A24 a)}$$

and

$$P'_m = \int \sin(2\pi m\, z/d_h)\, P(z)\, d_z \qquad \text{(A24 b)}$$

we relate P_m and P'_m with $f_{c,m}$ and $\Phi_{c,m}$ via

$$f_{c,m} = (P_m^2 + P'^2_m)^{1/2} \qquad \text{(A25)}$$

$$\Phi_{c,m} = \arctan(P'_m/P_m)/2\pi \quad \begin{cases} +0.5, \text{ if } P'_m \leq 0 \text{ and } P_m < 0 \\ 0, \text{ otherwise} \end{cases} \qquad \text{(A26)}$$

Our model for P(z) is considered to be valid if the experimentally determined parameters $\Phi_{c,m}$ and $f_{c,m}$ are in agreement with (A25) and (A26).

In most realistic distribution functions, a certain number of contemplated atoms will be randomly distributed, as discussed in this paper. This is equivalent to a separation of P(z) in two parts.

$$P(z) = (1-U)\{\sum_{i=1}^{N_G} c_i\, \delta(z-z_i)\} + U\{1/N_u \sum_{i=1}^{N_U} \delta(z-z_i)\} \qquad \text{(A27 a)}$$

$$= P_G(z) + P_R(z) \qquad \text{(A27 b)}$$

The sums are normalized such that $\int P(z)dz = 1$. In the first sum N_G is a small number (often $N_G = 1$) giving the total number of different,

significantly populated positions z_i where $c_i(\Sigma c_i \leq 1)$ defines the size of the individual fractions at z_i. The parameter U in both sums is defined by $U = N_U/N_A$ where N_A is the total number of sampled atoms (usually $N_A > 10^{10}$). The positions z_i of the N_U atoms are supposed to be occupied in a random fashion. The atomic positions are approximated by δ-functions. Inserting (A27 a) in (A23 b) it is obvious that to a very good approximation

$$U/N_U \sum_{i=1}^{N_U} \cos(2\pi m z_i/d_h) = U/N_U \sum_{i=1}^{N_U} \sin(2\pi m z_i/d_h) = 0 \qquad \text{(A28)}$$

since it represents a sum of sin/cos-functions with random phases and using (A24 a,b) we write

$$P_m = (1-U) \sum_{i=1}^{N_G} c_i \cos(2\pi m z_i/d_h) = (1-U)S_G \quad , \qquad \text{(A29 a)}$$

$$P'_m = (1-U) \sum_{i=1}^{N_G} c_i \sin(2\pi m z_i/d_h) = (1-U)S'_G \qquad \text{(A29 b)}$$

and obtain

$$f_{c,m} = (1-U)\sqrt{(S_G^2 + S_G'^2)} = (1-U)A_G \quad . \qquad \text{(A29 c)}$$

If we substitute the δ-function by a Gaussian distribution function which takes into account displacements of the atoms from thermal vibrations, we obtain

$$f_{c,m} = (1-U)A_G \cdot D_{WH} \qquad \text{(A30)}$$

Here we consider all thermal displacements at individual positions z_i having the same profile and

$$D_{WH} = \exp(-2\pi^2 m^2 \sigma^2) \qquad (A31)$$

represents the Debye-Waller temperature factor with

$$\sigma^2 = \langle u^2 \rangle / d_h^2 \qquad (A32)$$

where $\langle u^2 \rangle$ is the mean square vibrational amplitude of the atoms.

Thus, a decrease of the coherent fraction $f_{c,m}$ from the maximum value $f_{c,m} = 1$ can be caused by three factors

(1) Thermal vibrations, characterized by D_{WH}

(2) Occupation of multiple positions, characterized by A_G

(3) Random disorder, characterized by U.

A1.3 Calculation of fluorescence intensities and determination of coverage

The off-Bragg intensity I_s^o (in photons/s) of the fluorescence from the substrate atoms is given by

$$I_{Fs}^o = I_{FS} \cdot Q_s \cdot N_c/V_c \cdot (\sin\vartheta_s)^{-1} \cdot d_e \qquad (A33)$$

where Q_s is the cross-section of the incoming x-ray beam, N_c is the number of atoms per substrate lattice unit cell and V_c is the unit cell volume. The off-Bragg intensity I_{FA}^o from an adsorbate is

$$I_{FA}^o = I_{FA} \cdot Q_A \cdot N_A/A_s \cdot (\sin\vartheta_A)^{-1} \qquad (A34)$$

where N_A / A_s now denotes the number of adsorbate atoms N_A per surface unit cell and the unit cell area A_s, respectively, and beam cross-section

Q_A. The thickness d_e of the crystal which is sampled by XSW is given by equ. (A22 b).

The normalized fluorescence intensity I_{Fx}, where x stands for S (substrate) or A (adsorbate), is defined via

$$I_{Fx} = I_{\gamma x} \Delta\Omega_x / 4\pi \sigma_{px} \nu_{Fx} e_{Dx} \qquad (A35)$$

where $I_{\gamma x}$ is the primary intensity of the x-ray beam in photons/(s cm^2). The solid angle $\Delta\Omega$ is defined by the active area of the (fluorescence) detector and by its distance to the illuminated spot on the sample surface. The other three parameters are: partial cross sections (e.g. K-shell), σ_p; fluorescence probability ν_F; detector efficiency e_D (including loss due to absorption suffered by photons on the way to the detector).

Off-Bragg fluorescence counts A_{Fx}^o and fluorescence intensity are simply related by the measuring time t_m:

$$A_{Fx}^o = I_{Fx}^o \cdot t_m \qquad (A36)$$

We could determine e.g. the surface coverage

$$\Theta = N_A/A_s \qquad (A37)$$

of an adsorbate using (A35) and (A34). However, some experimental parameters like Q, I_γ and $\Delta\Omega$ can often not be determined with the necessary accuracy but using (A33) and (A34) leads to

$$\Theta = (A_A^o/A_S^o)(\sigma_{ps} \nu_{Fs} e_{Ds})/(\sigma_{pA} \nu_{FA} e_{DA})\ N_c/V_c\ d_e \qquad (A38)$$

when the fluorescence from the substrate and the adsorbate are recorded during the same measurement, since in this case $Q_S = Q_A$, $I_{\gamma S} = I_{\gamma A}$, $\Delta\Omega_S = \Delta\Omega_A$ and $\vartheta_S = \vartheta_A$. When photons scattered from the sample are recorded with an energy dispersive detector, fluorescence lines from substrate and overlayer are recorded in the same spectrum anyway and A^o_{FS} as well as A^o_{FA} can be obtained by least square fitting equ. (1) to the experimental data.

APPENDIX A2

The bond length (copper-adsorbate), l_A, and the distance z_{Ai} of an adsorbate atom normal to the surface (compare Fig. 14) are related by the following equations:

$$l_A = z_{A1} \tag{A39}$$

$$l_A = (z_{A2}^2 + (r_{Cu}^M)^2)^{1/2} \tag{A40}$$

$$l_A = (z_{A3}^2 + 4/3(r_{Cu}^M)^2)^{1/2} \tag{A41}$$

$$l_A = z_{A4}^2 + [a/2]^2 \tag{A42}$$

The position z_{A1} exhibits the largest and the positions z_{A3} and z_{A4} exhibit the smallest possible surface distance. Other positions with lower symmetry exhibit intermediate z_A values. The meaning and value of used constants are compiled in Table A1. A4 denotes the fourfold coordinated site on a (100) Cu surface.

Table A1: Constants and Notations

Meaning	Symbol	Value
Copper lattice constant	a	3.62 Å
Copper (111) lattice plane spacing	d_{111}	2.09 Å
Copper (200) lattice plane spacing	d_{200}	1.81 Å
Copper (hkl) lattice plane spacing	d_{hkl}	$3.62/(h^2+k^2+l^2)^{1/2}$ x Å
Metallic radius, copper	r^M_{Cu}	1.28 Å
Copper-Copper binding length	l	2.56 Å
A Monolayer on Cu(111)	$1\ ML_{111}$	1.76×10^{15} atoms cm^{-2}
A Monolayer on Cu(200)	$1\ ML_{200}$	1.53×10^{15} atoms cm^{-2}
Metallic radius, thallium	r^M_{Tl}	1.73 Å
Metallic radius, cadmium	r^M_{Cd}	1.49 Å
Copper Adsorbate binding length	l_A	$r_{Cu} + r_A$
Copper-Adsorbate metallic binding length	l^M_A	$r^M_{Cu} + r^M_A$
Difference to metallic binding length	Δl_A	$l_A - l^M_A$

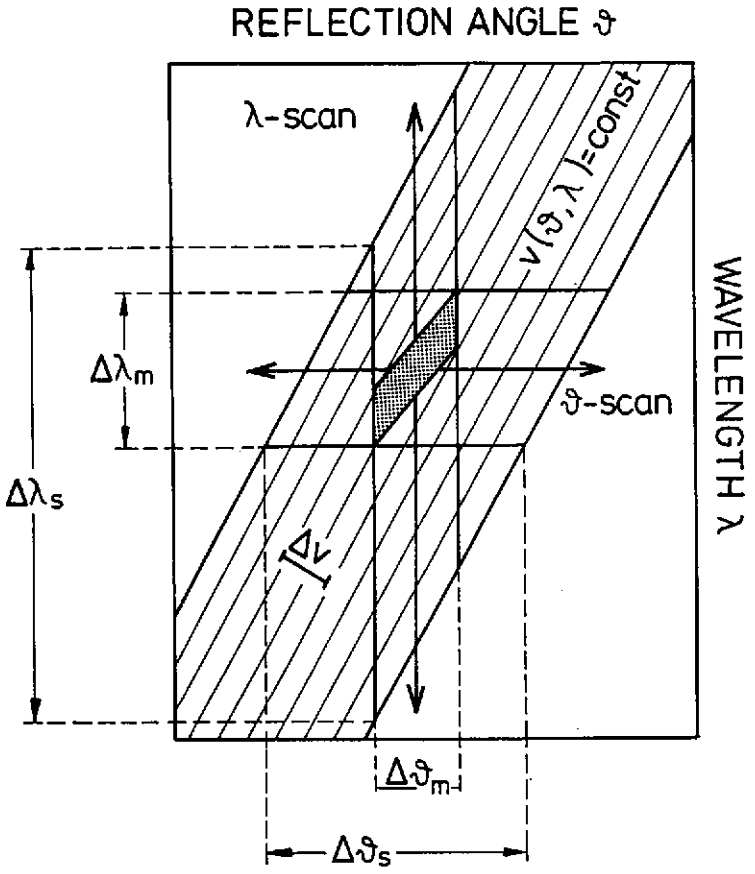

Fig. 1

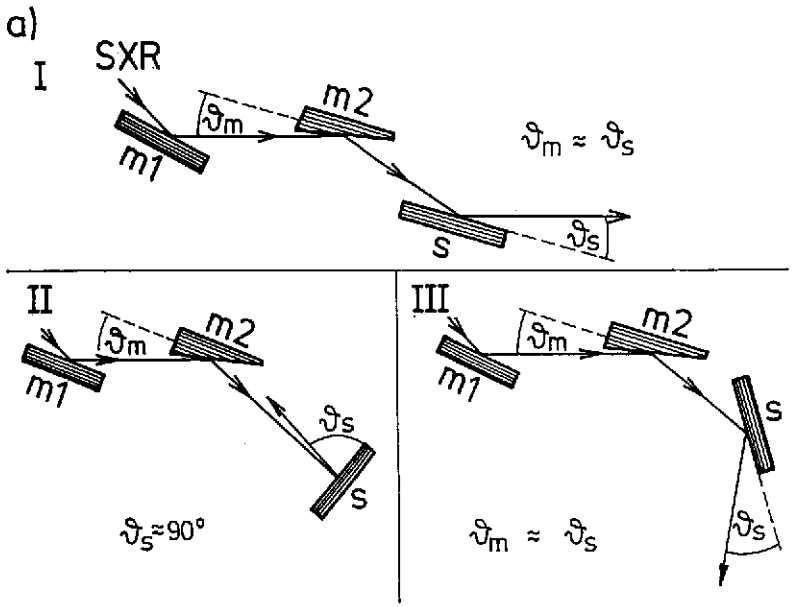
a)
I
SXR
m1
m2
ϑ_m
$\vartheta_m \approx \vartheta_s$
s
ϑ_s
II
m1
m2
ϑ_m
ϑ_s
s
$\vartheta_s \approx 90°$
III
m1
m2
ϑ_m
s
ϑ_s
$\vartheta_m \approx \vartheta_s$

Fig. 2a

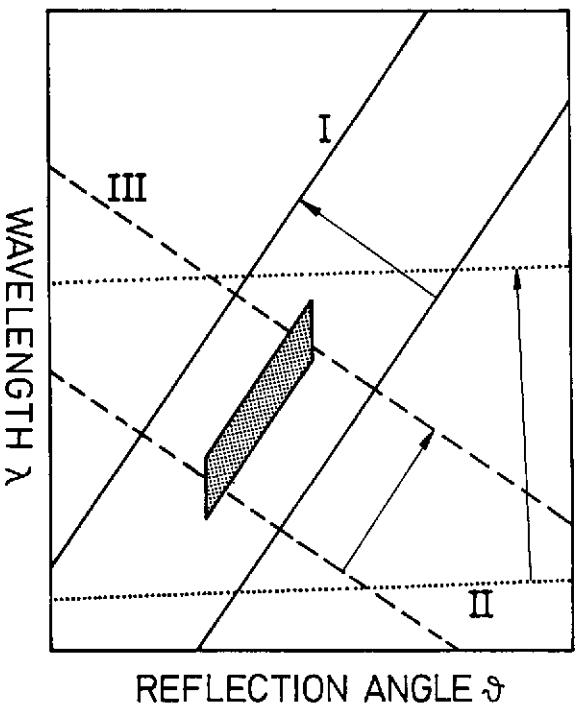
I
III
II
WAVELENGTH λ
REFLECTION ANGLE ϑ

Fig. 2b

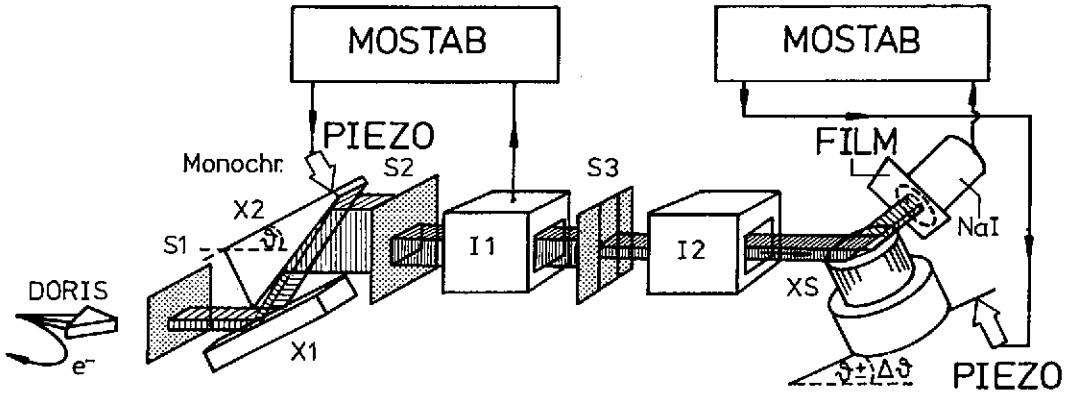
MOSTAB
MOSTAB
PIEZO
FILM
Monochr.
S2
S3
X2
S1
I1
I2
NaI
DORIS
XS
X1
PIEZO

Fig. 4

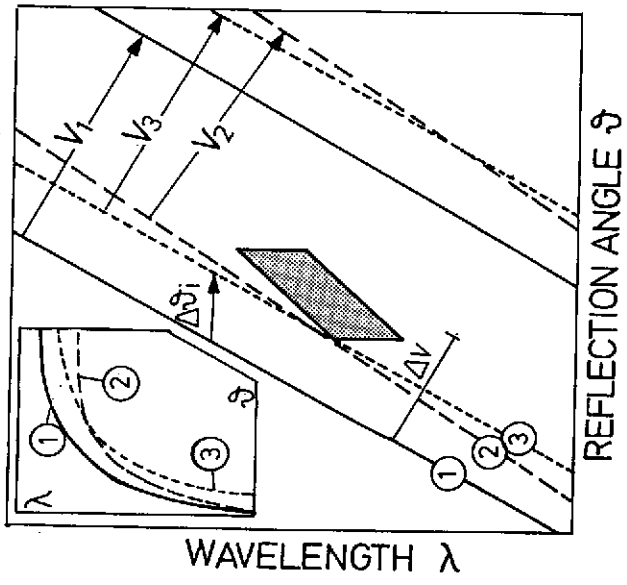
REFLECTION ANGLE ϑ
WAVELENGTH λ

Fig. 3

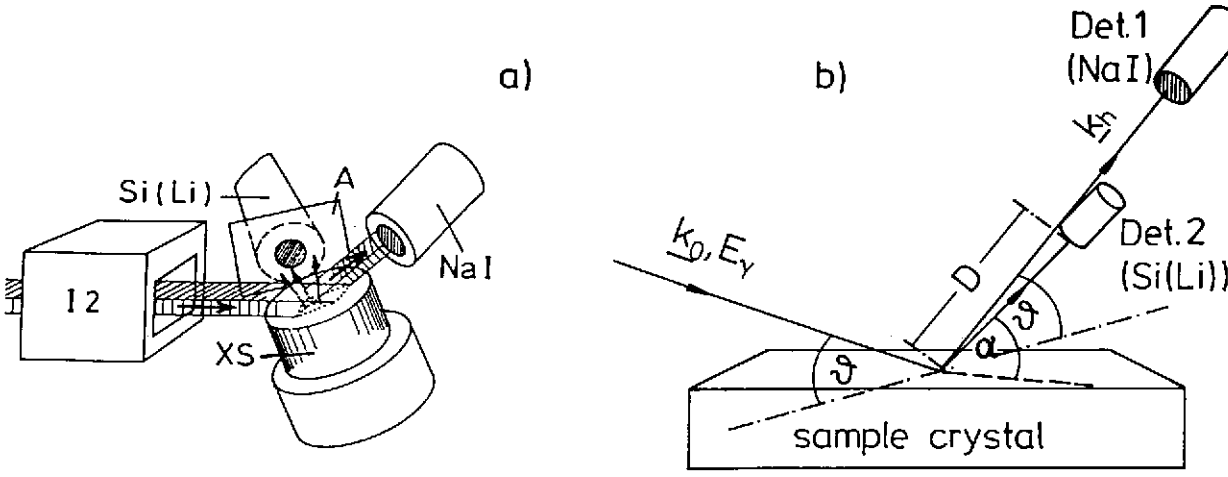
a)
Si(Li)
A
NaI
I 2
XS
b)
Det.1
(NaI)
Det.2
(Si(Li))
D
sample crystal

Fig. 6

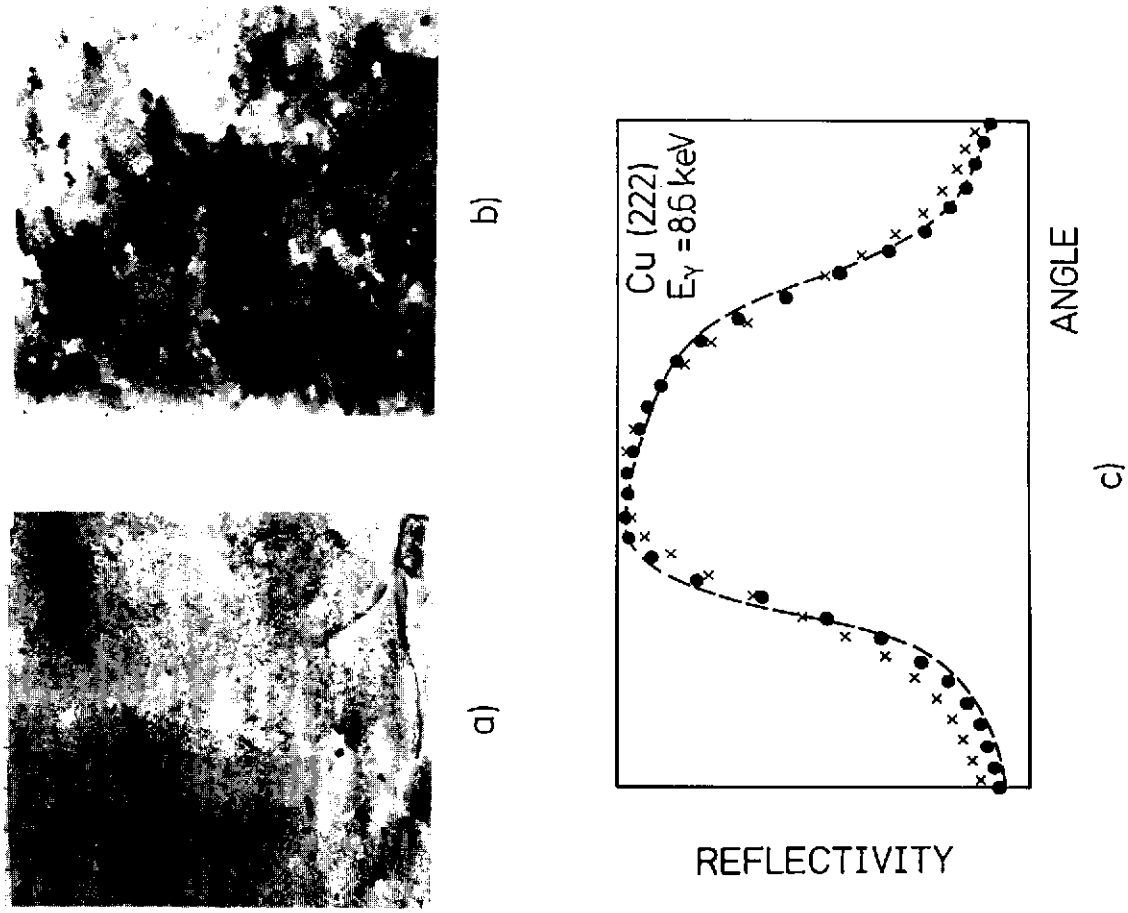
b)
a)
Cu (222)
Eγ =8.6 keV
ANGLE
c)
REFLECTIVITY

Fig. 5

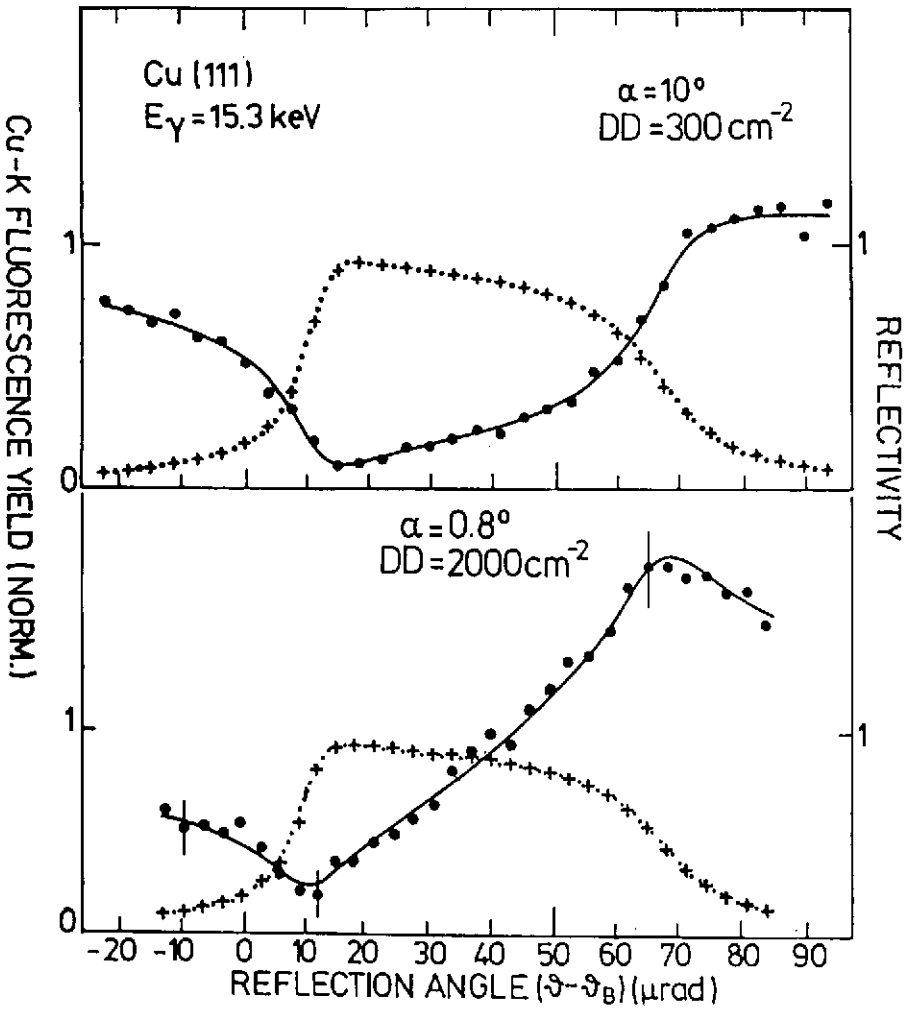
Cu (111)
Eγ = 15.3 keV
α = 10°
DD = 300 cm⁻²
α = 0.8°
DD = 2000 cm⁻²
Cu-K FLUORESCENCE YIELD (NORM.)
REFLECTIVITY
REFLECTION ANGLE (ϑ-ϑB) (μrad)
-20 -10 0 10 20 30 40 50 60 70 80 90
0
1

Fig. 7

Fig. 8

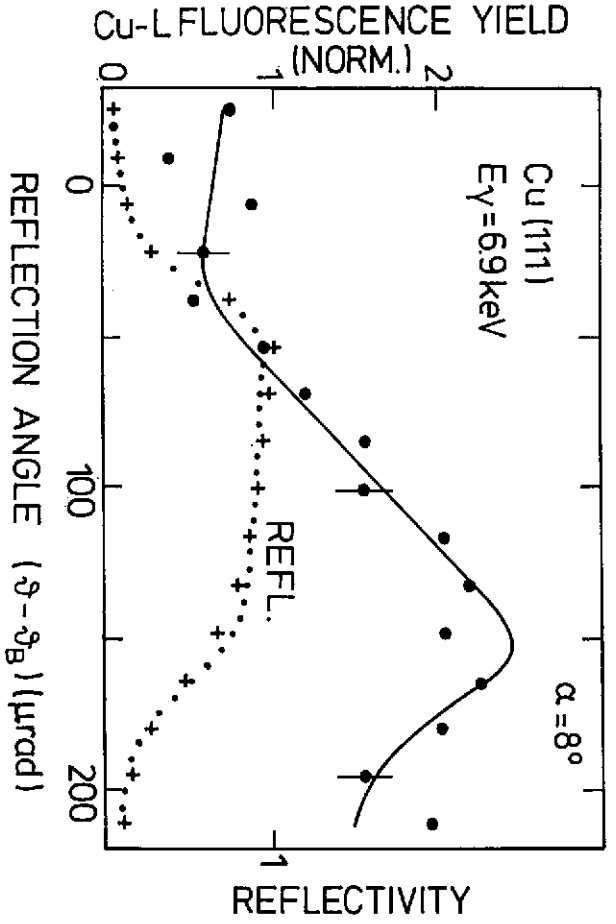
Cu-L FLUORESCENCE YIELD (NORM.)
Cu (111)
Eγ = 6.9 keV
REFL.
α = 8°
REFLECTION ANGLE (ϑ-ϑB) (μrad)
REFLECTIVITY
0
100
200
1
2

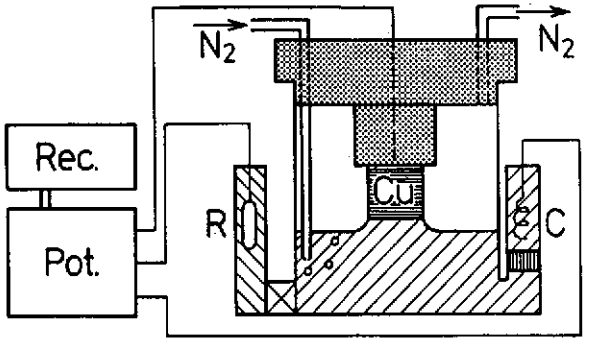
N2
N2
Rec.
Pot.
R
Cu
C

Fig. 9

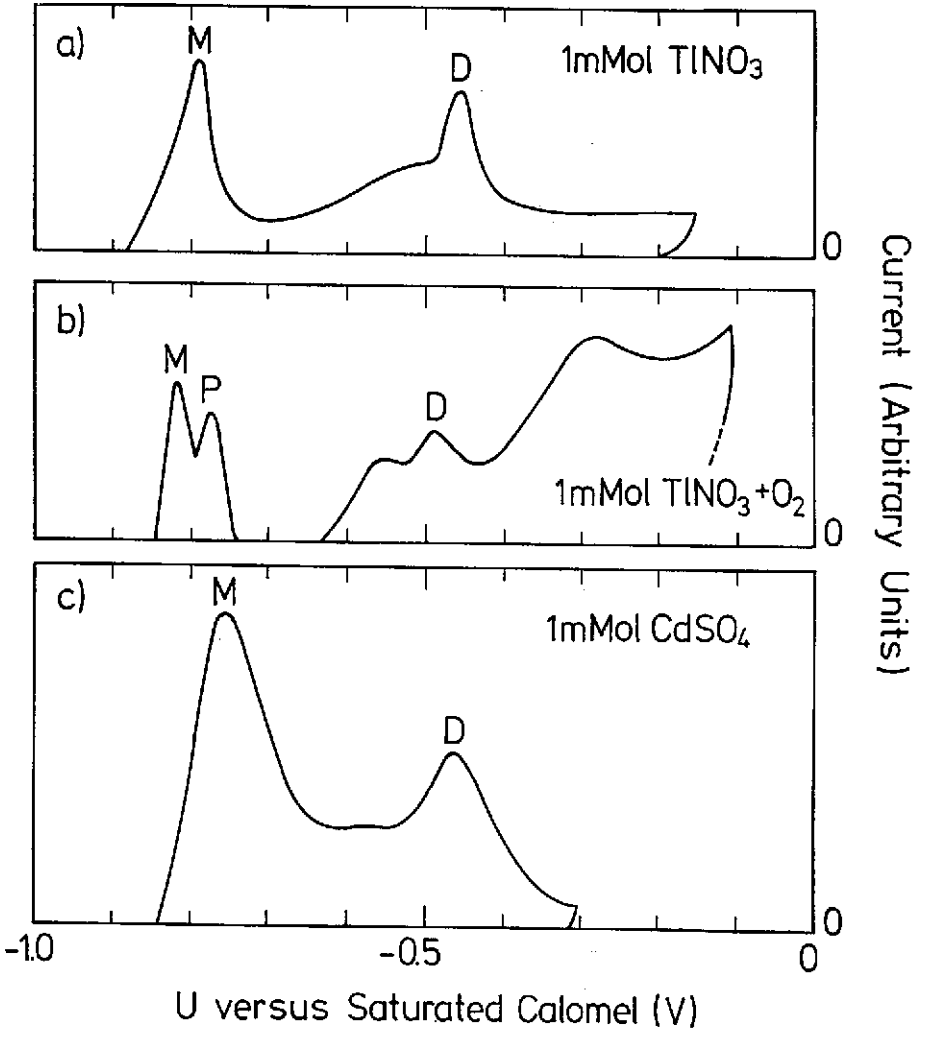
a)
M
D
1mMol TlNO3
0
b)
M
P
D
1mMol TlNO3+O2
0
c)
M
D
1mMol CdSO4
0
-1.0
-0.5
0
U versus Saturated Calomel (V)
Current (Arbitrary Units)

Fig. 10

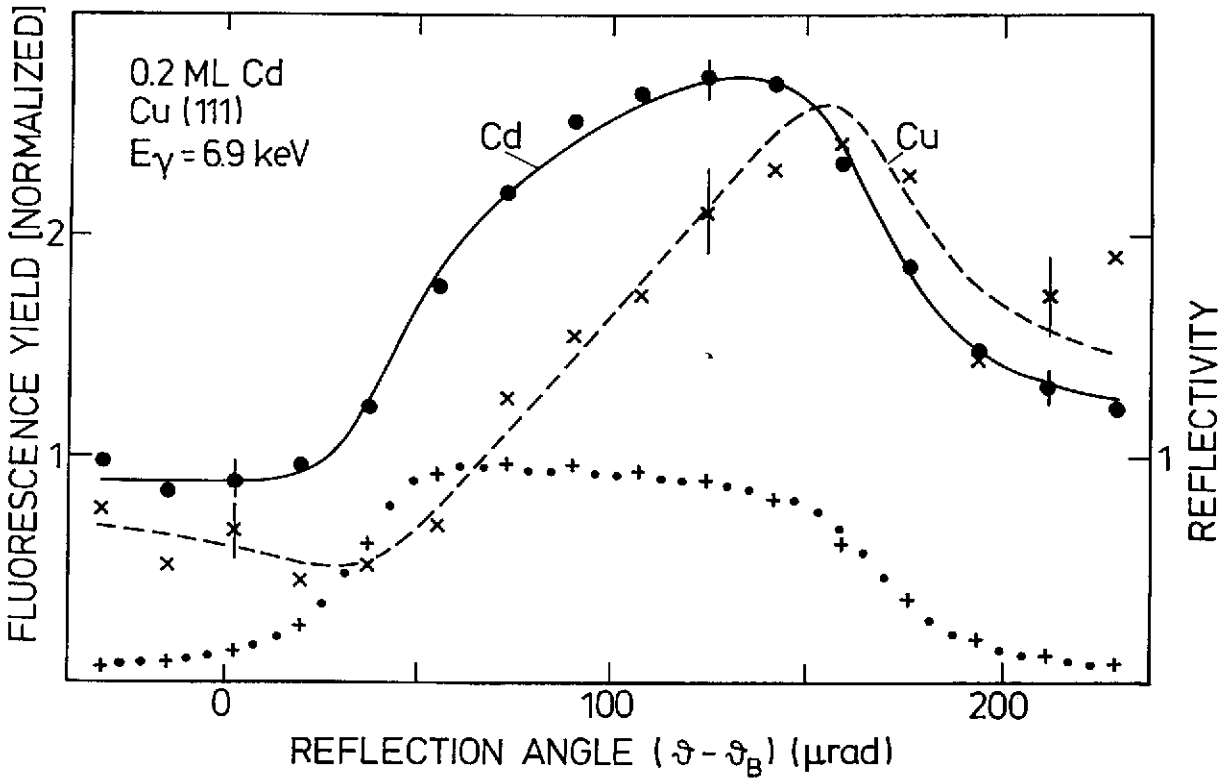
0.2 ML Cd
Cu (111)
Eγ = 6.9 keV
Cd
Cu
FLUORESCENCE YIELD [NORMALIZED]
REFLECTIVITY
2
1
1
0
100
200
REFLECTION ANGLE (ϑ - ϑB) (μrad)

Fig. 12

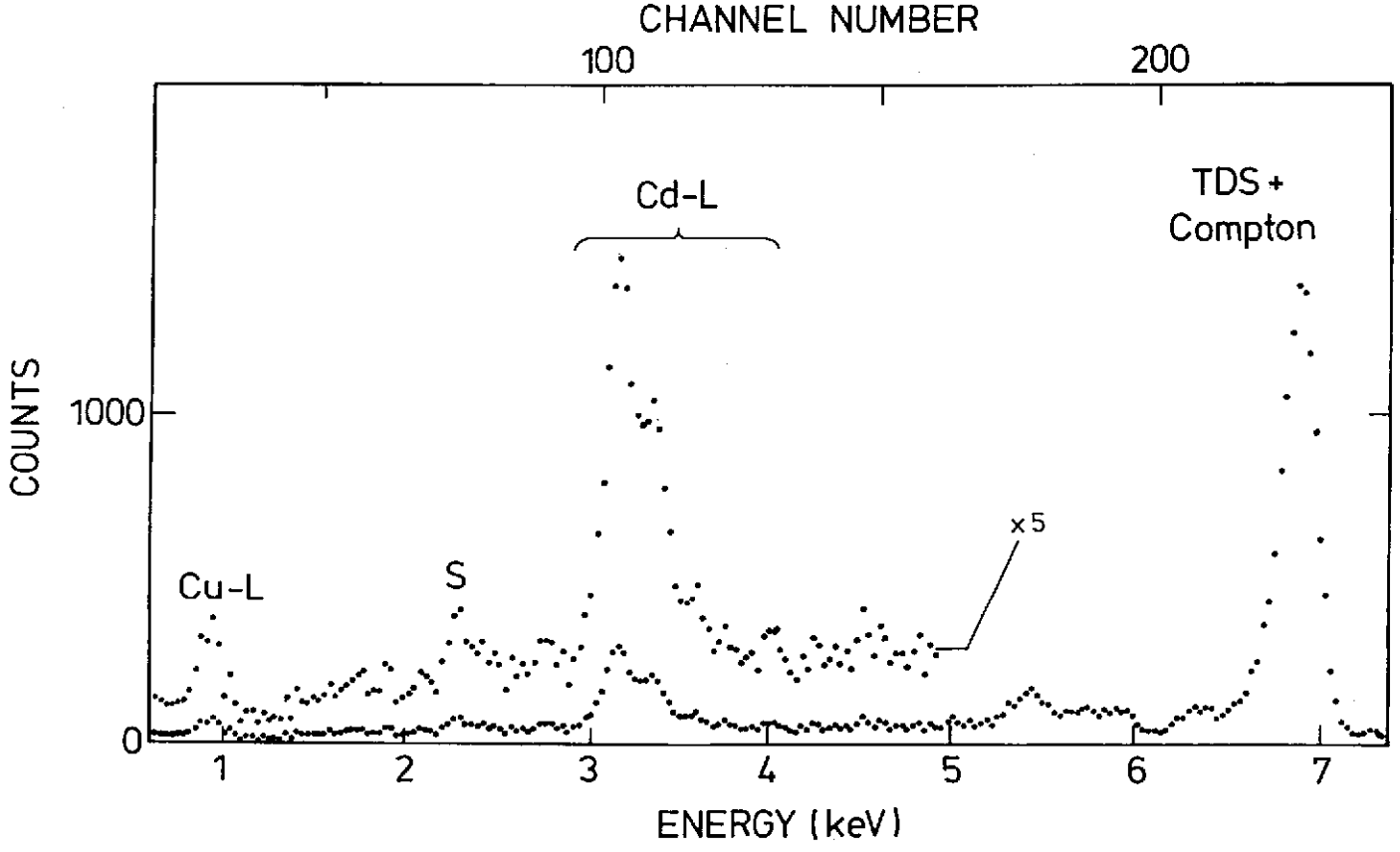
CHANNEL NUMBER
100
200
Cd-L
TDS +
Compton
COUNTS
1000
0
x5
Cu-L
S
1
2
3
4
5
6
7
ENERGY (keV)

Fig. 11

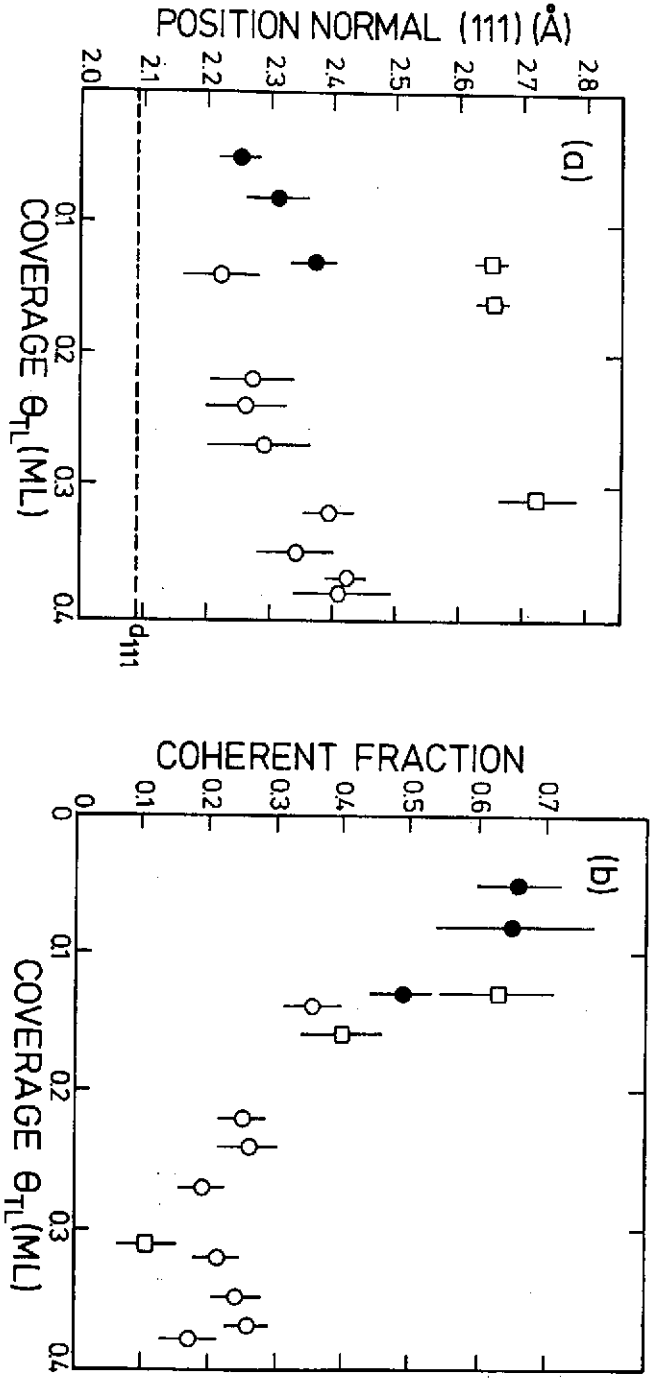
POSITION NORMAL (111) (Å)
2.0
2.1
2.2
2.3
2.4
2.5
2.6
2.7
2.8
(a)
COVERAGE θ_{TL} (ML)
0.1
0.2
0.3
0.4
d_{111}
COHERENT FRACTION
0
0.1
0.2
0.3
0.4
0.5
0.6
0.7
(b)
COVERAGE θ_{TL} (ML)
0.1
0.2
0.3
0.4

Fig. 13

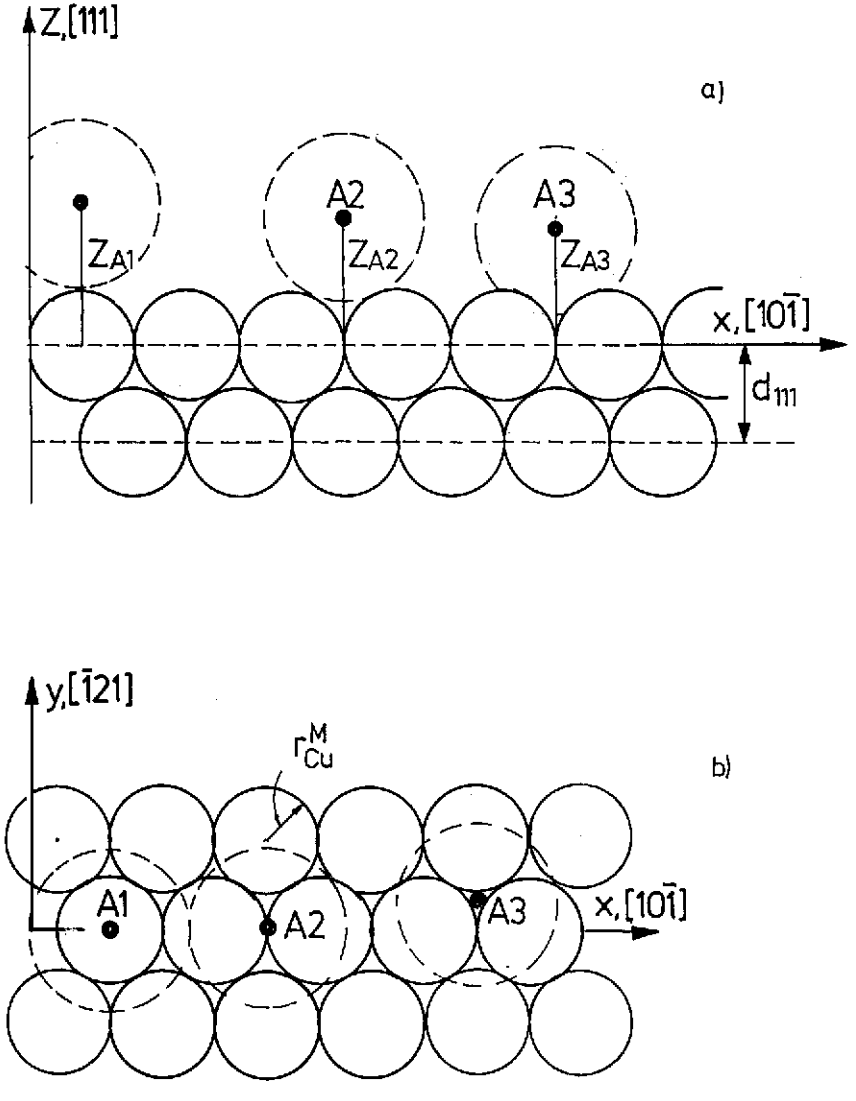
Z,[111]
a)
A2
A3
Z_{A1}
Z_{A2}
Z_{A3}
x,[10$\bar{1}$]
d_{111}
y,[$\bar{1}$21]
r^M_{Cu}
b)
A1
A2
A3
x,[10$\bar{1}$]

Fig. 14

Cu (111) surface plane

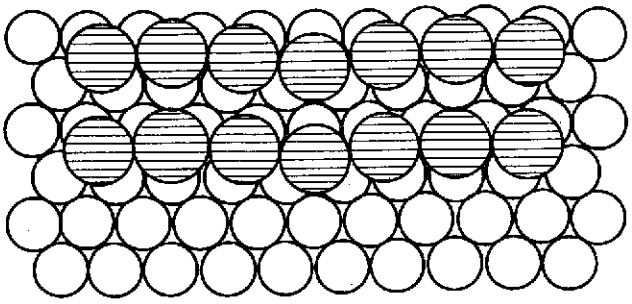

Fig. 15